2023 IEEE International Conference on Robotics and Automation (ICRA 2023)
May 29 - June 2, 2023. London, UK

A lightweight high-voltage boost circuit for soft-actuated micro-aerial-robots

Zhijian Ren, Jiahui Yang, Suhan Kim, Yi-Hsuan Hsiao, Jeffrey Lang, and Yufeng Chen*

***Abstract*— Flight is an energetically expensive task. While aerial insects can effortlessly fly through natural environments, achieving power autonomous flights in insect-scale robots remains a major challenge. In prior works, we developed soft-actuated insect-scale aerial robots that demonstrated unique capabilities such as in-flight collision recovery and somersaults. However, the soft dielectric elastomer actuators (DEAs) have low efficiency (<20%) and require a high driving voltage (>600 V). These properties represent formidable obstacles for soft aerial robots to achieve power autonomous flights. In this work, we developed a 127 mg boost circuit that can convert a 7.7 V DC input into a 600 V and 400 Hz output for driving a 120 mg DEA. It has an equivalent capacitance and resistance of 20 nF and 5 kΩ, respectively. The DEA is assembled into a 158 mg aerial robot, which can demonstrate liftoff while carrying the boost circuit as a payload. Although the robot remains tethered to an off-board power supply, this result represents a first step towards achieving power autonomy in soft aerial robots.**

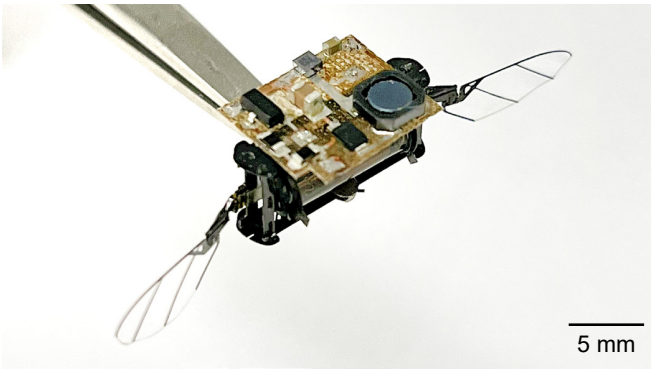

Fig. 1. An image of a 158 mg soft-actuated aerial robot that carries a 127 mg boost circuit. This insect-scale DEA-driven robot can demonstrate liftoff flights while carrying the circuit.

I. INTRODUCTION

Insects are ubiquitous in nature. Owing to their small sizes, insects can perform impressive and unique tasks such as climbing on walls, traversing the water surface, and pollinating flowers. While autonomous exploration of the natural environment seems effortless for insects, similarly sized robots struggle to achieve power autonomy due to a suite of major challenges. First, developing insect-scale (<1 g) robots requires microscale (0.01 – 0.1 g) structures, transmissions, and actuators. Second, lightweight power electronic circuits are required for driving micro-actuators that often need high voltages (>100 V). Third, compact energy sources such as batteries and solar cells need to be incorporated onboard. All these essential microrobotic components need to fit into an insect-scale system, which poses significant challenges in design, actuation, power electronics, and fabrication. In the past decade, advances in the abovementioned research areas have led to several power autonomous insect-scale robots. Huang et al. [1], [2] developed shape memory alloy (SMA) driven robots capable of terrestrial and aquatic locomotion. SMAs only require a low voltage (<10 V) and low frequency (<20 Hz) driving signal, hence it is easier to develop compact onboard electronics. However, the power density and controllability of SMAs are substantially smaller than that of insect muscles, which limit microrobot speed, maneuverability, and payload. To obtain higher bandwidth and power, other types of micro-actuators such as piezoelectric ceramics [3], polyvinylidene fluoride (PVDF) [4], and DEAs [5] have been applied in sub-gram terrestrial robots. Boost circuits capable of delivering 200 – 600 V driving signals have been developed for these high voltage actuators. These robots can carry a 0.5 – 1.0 g onboard battery and demonstrate power autonomous operation for 5 – 13 minutes [3], [4], [5].

Compared to aquatic and terrestrial locomotion, flight is substantially more energetically intensive. Achieving flight requires a lightweight airframe, power dense flight muscles, and compact electronics. While mesoscale (20 – 30 g) biomimetic flapping-wing robots [6], [7] have demonstrated agile power autonomous flights, insect-scale micro-aerial-vehicles (IMAVs) have not achieved full power autonomy. Lindsey et al. developed a motor-driven IMAV [8], [9], [10], [11] that has an elastic element for energy recovery. The 2.7 g robot demonstrated a lift-to-weight ratio of 1.4, but the net lift force remained insufficient for achieving liftoff flight with a onboard battery. The state-of-the-art IMAVs [12] are driven by piezoelectric actuators that have high bandwidth (>100 Hz), power density (>1 kW/kg) and efficiency (>80%). Karpelson et al. designed custom boost circuits [13] that use a bi-directional flyback topology to achieve a high step-up ratio (V_{out}/V_{in} >20) with moderate efficiency (∼30%). Based on this design, laser [14] and solar [15] powered IMAVs have been developed where the robots can demonstrate short (<1 s) liftoffs while carrying their boost circuits. However, these IMAVs cannot yet carry energy sources during flight.

This work was partially supported by the National Science Foundation (award number FRR-2202477), and the Research Laborartory of Electronics, MIT (award number: 2244181). Any opinions, findings, and conclusions expressed in this material are those of the authors and do not necessarily reflect the views of the National Science Foundation. Zhijian Ren and Suhan Kim are supported by the MathWorks Fellowship.

All authors are with the Research Laboratory of Electronics, Department of Electrical Engineering and Computer Science, Massachusetts Institute of Technology (MIT), Cambridge, MA USA, 02139.

*Yufeng Chen is the corresponding author, yufengc@mit.edu

In contrast to using rigid piezoelectric actuators, we developed IMAVs driven by soft DEAs [16], [17]. These soft-actuated IMAVs demonstrated insect-like functions such as collision resilience and acrobatic maneuvers, showing the unique promise of agile and robust soft robots. However, DEAs require a higher actuation voltage (600 V – 2000 V) and they have a lower transduction efficiency (15% – 30%). These shortcomings pose great challenges for developing onboard electronics in soft IMAVs.

In this work, we developed a 127-mg boost circuit for driving a 120 mg DEA at 400 Hz and 600 V. With an equivalent capacitance (C) and resistance (R) of 20 nF and 5 kΩ, the DEA consumes a capacitive ($\frac{1}{2}CV^2f$) and resistive (I^2R) power of 1.5 W and 0.6 W, respectively. Our circuit adapts a tapped-inductor boost topology, and we designed and fabricated a custom circuit using off-the-shelf components. The circuit receives a 7.7 V DC input with an average current of 0.31 A, and it converts this input into a 400 Hz and 600 V output for driving a DEA. To optimize the DEA and robot performance, we implemented pulse frequency modulation (PFM) for controlling the primary side MOSFET and maximizing the power transfer in the charging phase. Through experiments, we further designed a look-up table for controlling the discharging MOSFET so the output signal resembles a sinusoid. Furthermore, to simplify the circuit design, we characterized the robot flapping-wing performance under non-ideal driving waveforms. These results culminate in a liftoff demonstration where a 158-mg robot flies upward while carrying the 127-mg boost circuit (Fig. 1). Although the robot still cannot carry its battery, this work represents a first step towards achieving power autonomy in soft-actuated aerial robots.

II. DESIGN AND FABRICATION OF A LIGHTWEIGHT BOOST CIRCUIT

In this section, we describe key challenges of driving soft-actuated aerial robots and then present our circuit design and control methods. Our circuit takes in a 7.7 V DC input and drives a 20 nF capacitive load at 600 V and 400 Hz. Based on the circuit design, we fabricated a printed circuit board (PCB) through laser micromachining and soldered commercially available electronic components using the reflow method. Here, we also describe component selection and fabrication processes that lead to the 127 mg boost circuit.

A. Boost circuit design and control

1) Choice of circuit topology: In a prior work [16], we developed a 155 mg DEA-driven aerial robot that requires a sinusoidal driving waveform of 600 V and 400 Hz. While the DEA has favorable mechanical properties such as collision resilience [18] and long endurance [16], it imposes challenges from the perspective of developing a boost circuit. The DEA is modelled as a series resistor-capacitor (RC) network with an equivalent resistance and capacitance of 5 kΩ and 20 nF, respectively. Compared to piezoelectric-driven IMAVs [14], [15], DEAs require significantly higher voltage (from 200 V to 600 V) and peak power (from 0.1 W to 2.0 W) under a similar payload. These challenges motivate us to design a boost circuit that maximizes its output power while satisfying the stringent payload constraint.

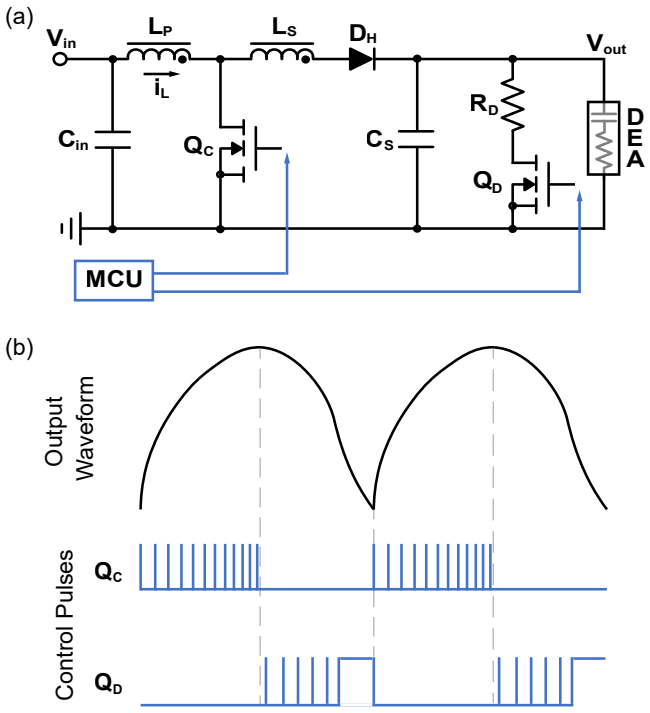

Fig. 2. Design and control of a tapped-inductor boost circuit. (a) An illustration of the circuit diagram. An offboard MCU controls the signals to switches Q_C and Q_D. (b) Illustration of the control signals to Q_C and Q_D during the DEA charging and discharging phases.

In recent years, several boost circuit topologies have been implemented for microscale systems. Park et al. [19] developed a 950-mg boost circuit that combines a step-up transformer and a capacitive ladder. The circuit can generate a high voltage of 4.45 kV and it enables electrostatic adhesion in a 10 g quadrotor. However, the capacitive ladder topology has lower power density and bandwidth than the traditional flyback topology [20], [21]. Most existing works [5], [14], [15], [22] adapt the flyback topology because it has a high step-up ratio (up to 100) and it consists of a small number of discrete components – making it well-suited for miniaturization. Hence, we chose to implement a tapped-inductor boost converter for driving the DEA.

Fig. 2a shows a schematic of our boost circuit design. The circuit transfers energy from the input (V_{in}) to the DEA (V_{out}). The switches Q_C and Q_D are implemented as NMOS transistors, where their control signals command the charging and the discharging phases, respectively. Fig. 2b illustrates a sample output waveform and the corresponding control signals, which are generated from a microcontroller (Arduino Uno). In the next subsections, we describe the design of control signals to Q_C and Q_D for optimizing the robot performance.

2) Circuit control in the DEA charging phase: In the charging phase, we maximize the energy delivered to the DEA through designing the control signal to Q_C. When Q_C

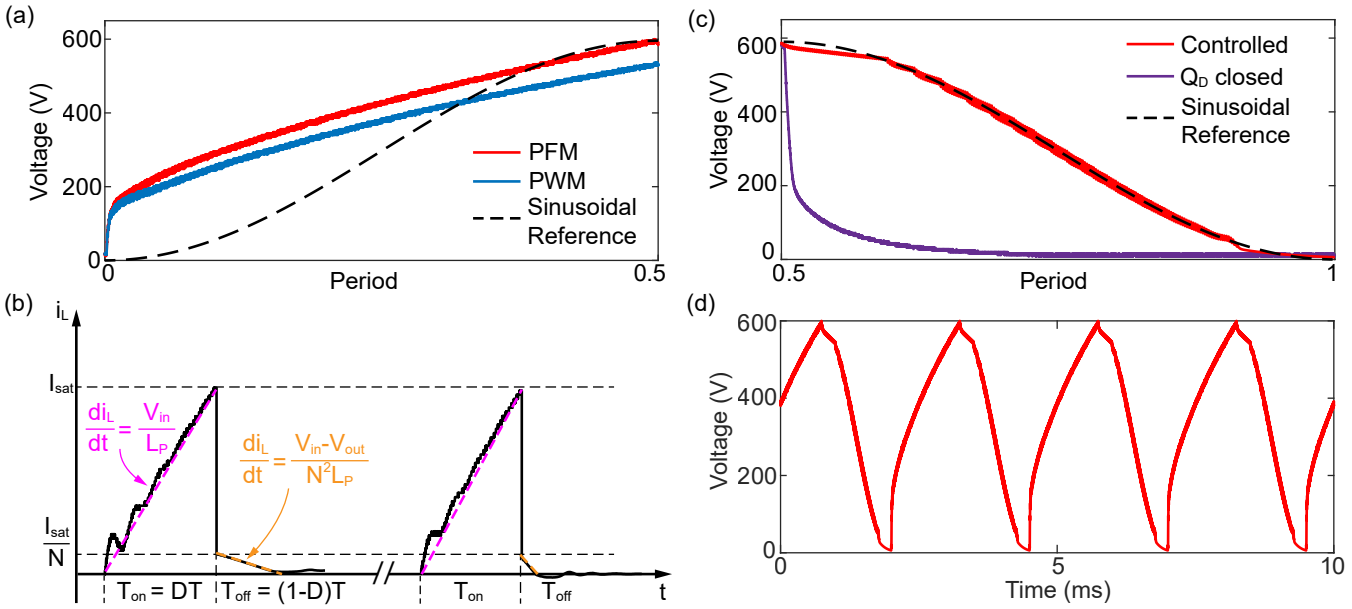

Fig. 3. Measurement of output voltage V_{out} in the DEA charging and discharging phases. (a) In the charging phase, the PFM implementation leads to a 10.3% increase of maximum V_{out}. (b) The primary inductor current decays faster as V_{out} increases. (c) In the discharging phase, the control signal to Q_D references a look-up table to ensure that V_{out} closely resembles a sinusoid. (d) Measured V_{out} when the circuit drives a DEA at 600 V and 400 Hz. In (a-d), the DC input voltage is 7.7 V.

is switched on, a current i_L charges the primary inductor L_p through the following equation:

$$L_p \frac{di_L}{dt} = V_{in} \tag{1}$$

Here we assume the inductor L_p and the switch Q_C have negligible resistance. We implemented a tapped-inductor through using a transformer with saturation current I_{sat}, turn ratio N, and primary inductance L_p. To maximize the amount of energy stored in the transformer, we set the switch-on time T_{on} such that the inductor current reaches I_{sat}:

$$T_{on} = I_{sat} L_p / V_{in} \tag{2}$$

After the primary inductor is fully charged, we switch off Q_C and the stored energy flows to the DEA through the diode D_H. This process is described by the following equation:

$$(L_p + L_s)\frac{di_L}{dt} = V_{in} - V_{out} \tag{3}$$

where the secondary inductance L_s relates to L_p through the relationship: $L_s = (N^2 - 1)L_p$. We command Q_C to remain open until the current i_L drops to 0. By solving equation (3), we can calculate the minimum switch-off time T_{off} as:

$$T_{off} = N I_{sat} L_p / (V_{out} - V_{in}) \tag{4}$$

After the transformer is fully discharged, we switch on Q_C and repeat the charging cycle. Equations (2) and (4) guide our design of control signals to Q_C. Specifically, we find that T_{on} is independent of the output voltage V_{out} so it is a constant value. In contrast, T_{off} reduces during the charging phase in which V_{out} gradually increases. Our MCU controls the duty ratio D that is defined as the fraction of time that Q_C is switched on:

$$D = \frac{T_{on}}{T_{on} + T_{off}} \tag{5}$$

We substitute equations (2) and (4) into (5) to obtain an expression for the optimized duty ratio D as a function of the output voltage V_{out}:

$$D = \frac{V_{out} - V_{in}}{V_{out} + (N-1)V_{in}} \tag{6}$$

The PFM method implements this optimized control signal, and it offers additional benefits such as reducing the ringing of inductor current [23]. Traditionally, PFM is implemented through feedback control where the MCU continuously measure i_L through a voltage divider [13], [22]. However, owing to the extreme payload limit, we implemented PFM through measuring i_L offline and then constructing a look-up table. Specifically, we used a current probe (TCP0030A, Tektronix) to measure T_{off} in each switching cycle. Based on the measurements, we compiled a look-up table in the MCU.

Fig. 3a shows the DEA charging phase where we compare an ideal sinusoidal waveform and the driving signals produced by PFM and PWM methods. Compared to PWM that has a fixed duty cycle D, our PFM approach shows a 10.3% increase of the peak output voltage. Fig. 3b illustrates T_{on} remains constant while T_{off} changes during the charging phase. Furthermore, we observe that the output voltage deviates from a pure sinusoidal waveform (Fig. 3a). In the DEA charging phase, we prioritize maximal power transfer over similarity to a pure sinusoid. We will quantify the influence

of higher harmonic components on robot performance in section III.

3) Circuit control in the DEA discharging phase: After the charging phase completes, we switch off Q_C and control the signals to Q_D for gradually discharging the DEA. When Q_D is switched on, a current flows through the discharge resistor R_D and the DEA voltage reduces. We control the signals to Q_D to achieve a sinusoidal discharging waveform. Fig. 3c compares the discharging waveforms where Q_D either remains closed or is being pulsed as shown in Fig. 2b. To achieve the discharging waveform in Fig. 3c (red), we constructed a circuit model in LTspice and then optimized the discharging control input in MATLAB. Based on the simulation result, we conducted discharging experiments and fine-tuned the control signals to Q_D. As shown in Fig. 3c, our discharging waveform closely resembles a pure sinusoidal with a normalized root-mean-square (rms) error of 1.43%. Finally, Fig. 3d shows the 600 V and 400 Hz driving signal that is produced by our circuit when the DC input voltage is 7.7 V.

B. Component selection and circuit fabrication

To fabricate the boost circuit (Fig. 2a), we selected off-the-shelf electronic components and laser micromachined a custom PCB board. The main challenge of this work is to assemble a circuit that can supply sufficient output power while satisfying the robot payload (∼150 mg). First, we chose a 60 mg transformer (LPR4012-202L, Coilcraft) that is capable of handling 2.5 W under a 7.7 V DC input. The primary inductance L_p and saturation current I_{sat} are 2 μH and 1.7 A, respectively. For most transformers, the component weight is proportional to the net stored energy ($\frac{1}{2}L_pI_{sat}^2$). To minimize weight while supplying a high power, our PFM control signals operate the transformer at high frequencies in the range of 500 kHz to 1 MHz. Furthermore, this transformer has a 1:10 turn ratio, which limits the voltage stress on Q_C to below 60 V.

Next, we selected the low-side and high-side switches Q_C and Q_D. Q_C is a fast-switching MOSFET (EPC2039, Efficient Power Conversion Corporation) that has a low drain-to-source resistance of 25 mΩ. Q_D is a high-voltage MOSFET (BSS127S-7, Diodes Incorporated) for discharging the current through R_D. In the discharging phase, 3.73 mJ of energy flows out of the DEA in 1.25 ms. This implies R_D needs to have a power rating of over 3 W. We connected two 1.5 W resistors in series to minimize the circuit weight. Table I lists all the circuit components and their corresponding mass.

Having selected the circuit components, we designed and fabricated a custom PCB through laser micromachining. Fig. 4a illustrates the fabrication process. First, we placed a 0.13 mm thick copper-clad FR4 sheet on an adhesive film (Gel-Pak, Hayward). Next, we selectively ablated the top copper layer (Fig. 4b) using a diode-pulsed laser (ProtoLaser U4, LPKF). Then we soldered the electronic components using reflow methods. Finally, we performed a laser release cut and removed the Gel-Film substrate layer. Fig. 4c shows the finished circuit that weighs 127 mg. The circuit requires three inputs: a 7.7 V DC supply (V_{in}) and the control signals to Q_C and Q_D .

TABLE I

CIRCUIT COMPONENTS AND MASS DISTRIBUTION

Component	Part	Mass (mg)
Coupled Inductor $\mathbf{L_P, L_S}$	LPR4012-202L	60
Low-side MOSFET $\mathbf{Q_C}$	EPC2039	4
High-side MOSFET $\mathbf{Q_D}$	BSS127S-7	8
Diode $\mathbf{D_H}$	RFU02VSM8STR	6
Input Capacitor $\mathbf{C_{in}}$	22 μF C0402	3
Stabilizing Capacitor $\mathbf{C_S}$	2.7 nF C0805	15
Discharging Resistors $\mathbf{R_D}$	1 kΩ R0603 (x2)	3
	Board and solder	28
	Total Mass	127

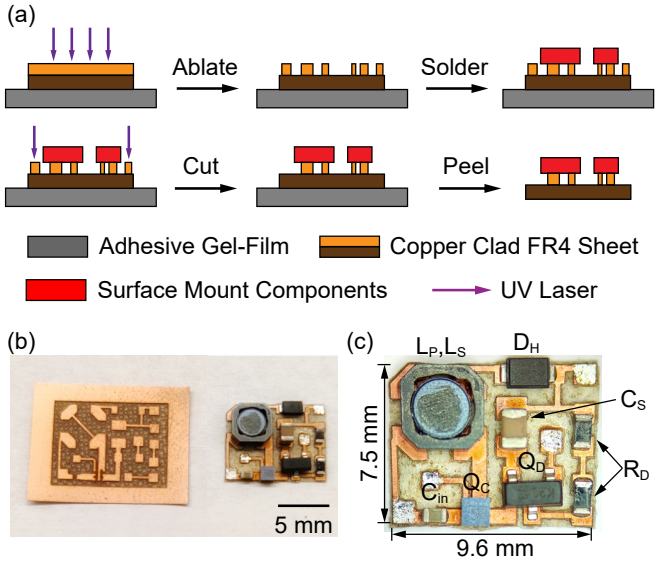

Fig. 4. Circuit fabrication. (a) Illustration of the circuit fabrication processes. A copper-clad FR4 template is laser ablated, and then electronic components are soldered onto the board. (b) An image of two circuits before and after populating the components. (c) A photo of the 127 mg finished circuit that has a dimension of 9.6 mm × 7.5 mm.

III. Experimental Characterization of the Boost Circuit and IMAV Liftoff Demonstration

In this section, we present two types of experiments that characterize the robot performance when it is driven by the boost circuit. First, we performed static flapping-wing experiments and quantified the robot performance change due to higher harmonic components in a non-ideal driving waveform. We found the robot's net lift force is proportional to the magnitude of the fundamental harmonic component. Second, we conducted liftoff experiments where the robot is driven by the boost circuit. The robot can achieve a lift-to-weight ratio of 2.03:1, and it further demonstrates liftoff while carrying the circuit.

A. Static flapping-wing experiments

We conducted static flapping-wing experiments by using a 158 mg robot. As described in our prior work [16], [17], the robot's net lift force is proportional to the amplitude of

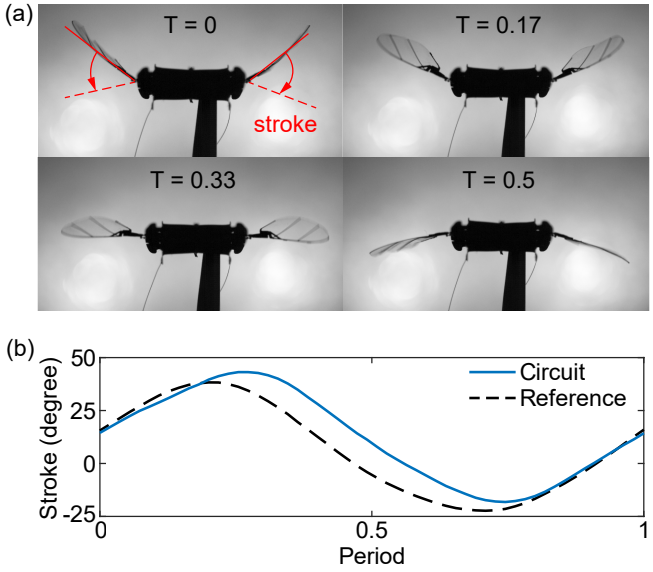

Fig. 5. Experimental characterization of robot flapping-wing kinematics. The time T is normalized to one flapping period. (a) An image sequence that shows the robot flapping-wing motion at 400 Hz. (b) Comparison of the measured (right wing) stroke motions when the robot is driven by the boost circuit (blue) or an amplifier (black).

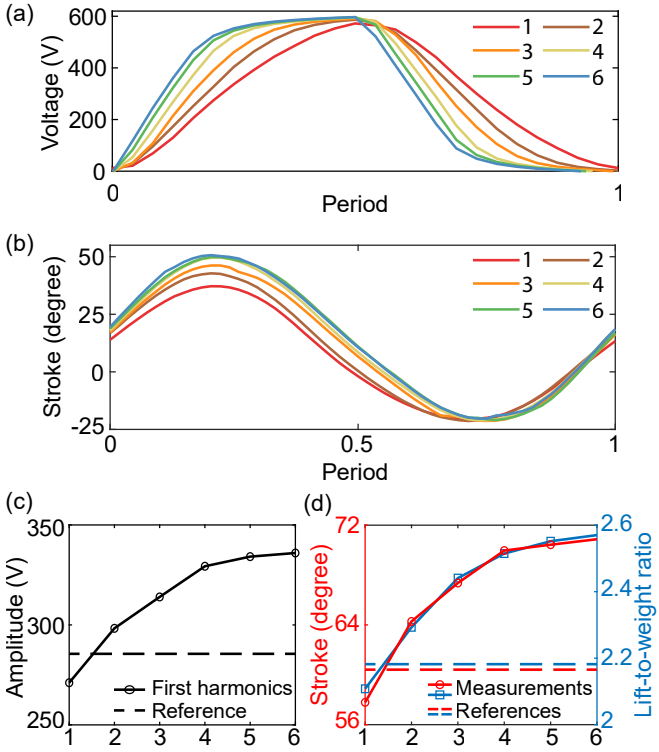

Fig. 6. Influence of driving signal distortion on flapping-wing kinematics and lift production. (a) Six distorted driving signals. (b) The measured (right wing) stroke motions that correspond to the waveforms in (a). (c) Voltage amplitude of the fundamental harmonic corresponding to the driving signals in (a). (d) Robot (right wing) stroke motion amplitude and lift-to-weight ratio corresponding to the driving signals in (a). In (c-d), the dashed lines indicate the corresponding values from a sinusoidal driving signal.

its wing stroke motion. Fig. 5a and Supplementary Video part 1 show half of a flapping-wing period where the robot is driven by the boost circuit. In this experiment, the DC input voltage is 7.5 V, and the output waveform has a peak voltage of 590 V and a frequency of 400 Hz. The tracked wing stroke kinematics is shown in Fig. 5b.

To quantify the influence of higher harmonic components on lift force production, we drove the same robot using a high voltage amplifier (Trek 2220, Advanced Energy Industries, Inc). First, we commanded a sinusoidal signal that has the same maximum voltage. The measured wing stroke motion (black curve in Fig. 5b) shows a similar amplitude compared to that of the boost circuit (blue curve in Fig. 5b), suggesting the circuit-driven robot can generate a similar lift force. However, there are noticeable differences between the two cases. When the robot is driven by the boost circuit, the waveform distortion in the charging phase (Fig. 3a) causes asymmetry between the wing upstroke and downstroke motion. Specifically, we observe that the robot's upstroke motion becomes 5% slower.

To investigate the influence of waveform distortion on lift force production, we designed 6 distorted driving signals and applied them to the robot. Fig. 6a shows the 6 signals where they have the same mean and maximum values. The tracked wing stroke kinematics are shown in Fig. 6b. For each flapping-wing experiment, we calculated the fundamental harmonic amplitudes associated with the driving signal (Fig. 6c) and the stroke motion (Fig. 6d). Fig. 6c-d show that a higher level of distortion leads to an increase of the wing stroke amplitude. The dashed lines in Fig. 6c-d show the fundamental harmonic amplitudes associated with a sinusoidal driving function of the same peak voltage. Based on these results, we further measured the robot lift force for each test case. Fig. 6d shows the robot lift-to-weight ratio increases from 2.10 to 2.55 when waveform distortion increases.

This result has two major takeaways. First, the DEAs are robust against non-sinusoidal driving waveforms. Second, under the same maximum voltage, the driving waveform that has the largest fundamental harmonic can generate the largest lift force. Future works should optimize the robot lift force by designing a driving waveform that has a large fundamental harmonic.

B. Robot liftoff demonstrations

We conducted two liftoff demonstrations and measured the robot lift force when it is driven by the boost circuit. Fig. 7a shows the liftoff experimental setup in which the robot is mounted on a takeoff stand. The stand is balanced around a pivot point. If the robot lift force exceeds the weight, then the robot ascends upward. We recorded the liftoff motion using a high-speed camera (VEO 710, Phantom) and extracted the net lift force using an existing method [18].

In the first experiment (Fig. 7b), we placed the boost circuit offboard and mounted a 120 mg payload on the robot. The boost circuit receives a 7.7 V DC input and outputs a 600 V and 400 Hz driving signal. The amplitude of the signal's DC and fundamental harmonics are 321 V and 248

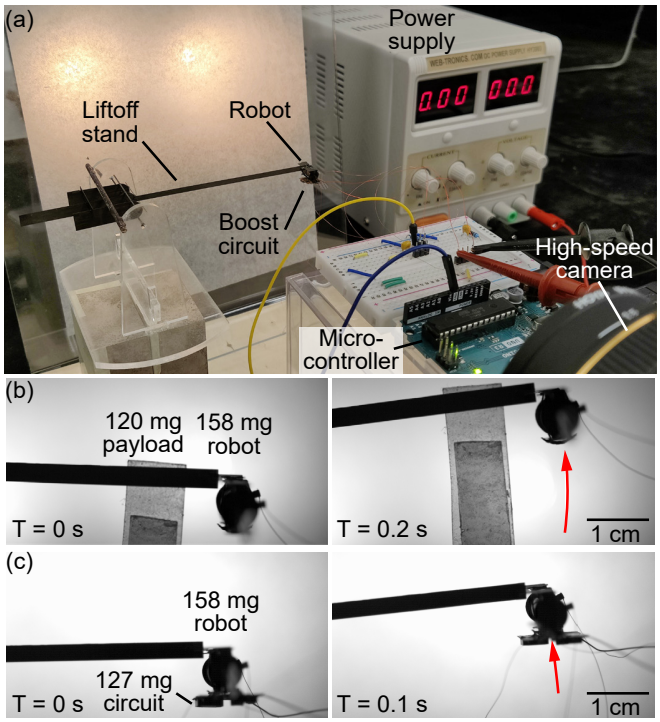

Fig. 7. Liftoff demonstrations of a 158 mg robot driven by the 127 mg boost circuit. (a) An image of the experimental setup. (b) Two consecutive images that show a robot liftoff where it carries a 120 mg payload. (c) Two consecutive images that show the robot lifts off while carrying a 127 mg boost circuit.

V, respectively. Under this condition, the robot's wing stroke amplitude is 60.1°. The robot demonstrates liftoff, and it reaches a height of 2 cm in 0.2 s (Fig. 7b and Supplementary Video part 2). Based on this experiment, we measured a robot lift-to-weight ratio of 2.03:1.

Next, we attached the 127 mg boost circuit beneath the robot airframe. We performed another liftoff experiment at the same driving condition, and the robot lifts upward by 1 cm in 0.1 s (also shown in Supplementary Video part 3). Compared to the previous liftoff experiment, the robot lift-to-weight ratio reduces to 1.98:1. This small lift reduction is caused by the tension from the power tether. To reduce the circuit resistance in the primary path, we connected 33 gauge wire from the DC power supply to the boost circuit. This wire has a substantially higher tension compared to the 43 gauge wire that connects to the DEA. Supplementary Video part 3 shows the robot is pulled by the power tether after 0.1 s. This issue could be solved in the future when an onboard battery replaces the offboard power supply. In summary, this experiment demonstrates a brief liftoff in which the 158 mg robot ascends upward while carrying a 127 mg boost circuit.

IV. DISCUSSION AND CONCLUSION

In this work, we demonstrated the first liftoff of a soft-actuated aerial robot that carries its own boost circuit. The 127 mg circuit has a tapped inductor boost converter topology, and it converts a 7.7 V DC input into a 600 V and 400 Hz driving waveform for the DEA. We micromachined the

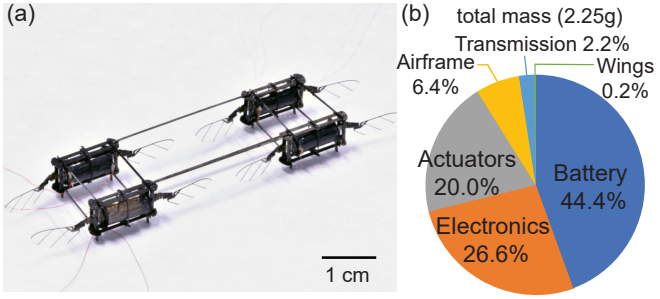

Fig. 8. Future outlook on power autonomous soft-actuated aerial robots. (a) An image of a 680 mg, 4-module robot that has over 1.5 g of payload [16]. (b) Distribution of total robot mass as predicted for the final, fully autonomous soft IMAV.

circuit board using a diode-pulsed laser and then soldered electronic components through the reflow techniques. To maximize the circuit's output power, we used the PFM method to control the switch Q_C in the charging phase. In the discharging phase, we implemented a lookup table such that the output waveform resembles a sinusoid. We further characterized the robot performance under non-ideal driving inputs and demonstrated a maximum robot lift-to-weight ratio of 2.55. These results enabled the robot to carry the boost circuit and achieve tethered liftoff under a 7.7 V DC input.

Compared to existing boost circuit designs [14], [15] for sub-gram aerial robots, our circuit supplies substantially higher voltage (600 V compared to 200 V) and power (2 W compared to 0.1 W) under a similar weight constraint. On one hand, this shows the disadvantage of DEAs compared to piezoelectric ceramic actuators due to lower efficiency and the requirement of higher voltages. On the other hand, DEAs tolerate non-ideal driving waveforms and maintain similar output forces. This advantage simplifies the circuit design and reduces the corresponding weight and size.

This liftoff result represents exciting progress for soft-actuated aerial robots, but it is limited in several key aspects. First, the robot cannot carry its energy sources and onboard computation. Second, the system efficiency is low (<10%) due to a lack of energy recycling. In every actuation cycle, the energy stored in the DEA is completely discharged through the resistor R_D. Future works on power electronics design should tackle these limitations. Fig. 8 illustrates our longer-term vision of developing a fully autonomous soft-actuated robot. Our new robot will consist of 4 modules, weigh 0.7 g, and have a net payload of 1.5 g (Fig. 8a). The total robot mass and its component mass distribution is shown in Fig. 8b. The robot will carry a 0.6 g boost circuit and 1 g battery. The DEAs will consume approximately 0.6 W during hovering flight, and the boost circuit will have a higher efficiency of 20% - 25% through implementing charge recycling. With a larger payload and more efficient boost circuit design, we envision future soft-actuated aerial robots will achieve fully autonomous flights and demonstrate unique insect-like functions.

REFERENCES

[1] X. Huang, K. Kumar, M. K. Jawed, A. M. Nasab, Z. Ye, W. Shan, and C. Majidi, "Chasing biomimetic locomotion speeds: Creating untethered soft robots with shape memory alloy actuators," *Science Robotics*, vol. 3, no. 25, p. eaau7557, 2018.

[2] X. Huang, "Untethered soft robots with shape memory alloy for dynamic locomotion," Ph.D. dissertation, Carnegie Mellon University, 2020.

[3] B. Goldberg, R. Zufferey, N. Doshi, E. F. Helbling, G. Whittredge, M. Kovac, and R. J. Wood, "Power and control autonomy for high-speed locomotion with an insect-scale legged robot," *IEEE Robotics and Automation Letters*, vol. 3, no. 2, pp. 987–993, 2018.

[4] J. Liang, Y. Wu, J. K. Yim, H. Chen, Z. Miao, H. Liu, Y. Liu, Y. Liu, D. Wang, W. Qiu *et al.*, "Electrostatic footpads enable agile insect-scale soft robots with trajectory control," *Science Robotics*, vol. 6, no. 55, p. eabe7906, 2021.

[5] X. Ji, X. Liu, V. Cacucciolo, M. Imboden, Y. Civet, A. El Haitami, S. Cantin, Y. Perriard, and H. Shea, "An autonomous untethered fast soft robotic insect driven by low-voltage dielectric elastomer actuators," *Science Robotics*, vol. 4, no. 37, p. eaaz6451, 2019.

[6] M. Karásek, F. T. Muijres, C. De Wagter, B. D. Remes, and G. C. De Croon, "A tailless aerial robotic flapper reveals that flies use torque coupling in rapid banked turns," *Science*, vol. 361, no. 6407, pp. 1089–1094, 2018.

[7] Z. Tu, F. Fei, and X. Deng, "Untethered flight of an at-scale dual-motor hummingbird robot with bio-inspired decoupled wings," *IEEE Robotics and Automation Letters*, vol. 5, no. 3, pp. 4194–4201, 2020.

[8] L. L. Hines, V. Arabagi, and M. Sitti, "Free flight simulations and pitch and roll control experiments of a sub-gram flapping-flight micro aerial vehicle," in *2011 IEEE International Conference on Robotics and Automation*. IEEE, 2011, pp. 1–7.

[9] L. Hines, V. Arabagi, and M. Sitti, "Shape memory polymer-based flexure stiffness control in a miniature flapping-wing robot," *IEEE Transactions on Robotics*, vol. 28, no. 4, pp. 987–990, 2012.

[10] L. Hines, D. Campolo, and M. Sitti, "Liftoff of a motor-driven, flapping-wing microaerial vehicle capable of resonance," *IEEE Transactions on Robotics*, vol. 30, no. 1, pp. 220–232, 2013.

[11] L. Hines, D. Colmenares, and M. Sitti, "Platform design and tethered flight of a motor-driven flapping-wing system," in *2015 IEEE international conference on robotics and automation (ICRA)*. IEEE, 2015, pp. 5838–5845.

[12] K. Y. Ma, P. Chirarattananon, S. B. Fuller, and R. J. Wood, "Controlled flight of a biologically inspired, insect-scale robot," *Science*, vol. 340, no. 6132, pp. 603–607, 2013.

[13] M. Karpelson, G.-Y. Wei, and R. J. Wood, "Driving high voltage piezoelectric actuators in microrobotic applications," *Sensors and actuators A: Physical*, vol. 176, pp. 78–89, 2012.

[14] J. James, V. Iyer, Y. Chukewad, S. Gollakota, and S. B. Fuller, "Liftoff of a 190 mg laser-powered aerial vehicle: The lightest wireless robot to fly," in *2018 IEEE International Conference on Robotics and Automation (ICRA)*. IEEE, 2018, pp. 3587–3594.

[15] N. T. Jafferis, E. F. Helbling, M. Karpelson, and R. J. Wood, "Untethered flight of an insect-sized flapping-wing microscale aerial vehicle," *Nature*, vol. 570, no. 7762, pp. 491–495, 2019.

[16] Z. Ren, S. Kim, X. Ji, W. Zhu, F. Niroui, J. Kong, and Y. Chen, "A high-lift micro-aerial-robot powered by low-voltage and long-endurance dielectric elastomer actuators," *Advanced Materials*, vol. 34, no. 7, p. 2106757, 2022.

[17] Y. Chen, H. Zhao, J. Mao, P. Chirarattananon, E. F. Helbling, N.-s. P. Hyun, D. R. Clarke, and R. J. Wood, "Controlled flight of a microrobot powered by soft artificial muscles," *Nature*, vol. 575, no. 7782, pp. 324–329, 2019.

[18] Y. Chen, S. Xu, Z. Ren, and P. Chirarattananon, "Collision resilient insect-scale soft-actuated aerial robots with high agility," *IEEE Transactions on Robotics*, vol. 37, no. 5, pp. 1752–1764, 2021.

[19] S. Park, D. S. Drew, S. Follmer, and J. Rivas-Davila, "Lightweight high voltage generator for untethered electroadhesive perching of micro air vehicles," *IEEE Robotics and Automation Letters*, vol. 5, no. 3, pp. 4485–4492, 2020.

[20] "Small, high-voltage boost converters," Maxim Semiconductor Application Note 1109, 2002.

[21] N. Vazquez, L. Estrada, C. Hernandez, and E. Rodriguez, "The tapped-inductor boost converter," in *2007 IEEE International Symposium on Industrial Electronics*. IEEE, 2007, pp. 538–543.

[22] M. Karpelson, G.-Y. Wei, and R. J. Wood, "Milligram-scale high-voltage power electronics for piezoelectric microrobots," in *2009 IEEE international conference on robotics and automation*. IEEE, 2009, pp. 2217–2224.

[23] U. Sengupta, "Pwm and pfm operation of dc/dc converters for portable applications," in *TI Power Supply Design Seminar*, vol. 1700, 2007.